An integrated 3D dynamic FE vehicle-track model in elasto-plasticity to investigate short pitch corrugation under cyclic wheel loads

Li, Shaoguang; Naeimi, Meysam; He, Chunyan; Dollevoet, Rolf; Li, Zili

Important note
To cite this publication, please use the final published version (if applicable).
Please check the document version above.

An integrated 3D dynamic FE vehicle-track model in elasto-plasticity to investigate short pitch corrugation under cyclic wheel loads

Shaoguang Li [a,b], Meysam Naeimi [a], Chunyan He [a], Rolf Dollevoet [a], Zili Li [a,*]

[a] *Delft University of Technology, Faculty of Civil Engineering and Geosciences, Section of Railway Engineering, Stevinweg 1, 2628 CN Delft, the Netherlands*
[b] *Eurailscout Inspection & Analysis, Berkenweg 11, Amersfoort 3818 LA, the Netherlands*

ABSTRACT

The mechanism of rail short pitch corrugation has remained elusive in the past. The damage mechanisms of the corrugation are reported to be differential wear or plastic deformation. The former has been extensively studied, while the plastic deformation, especially under multiple wheel passages has been seldom studied. To uncover the facts behind it, an integrated dynamic vehicle-track model with the rail material treated in elasto-plasticity is developed. Further, a novel method which can simulate the material deformation under cyclical axle loads is proposed. This method is used to study the rail material response at corrugation. Our research found that for the cases studied, the rail material undergoes cyclic plastic deformation at corrugation peaks only for a limited number of cycles (2–4 cycles) before reaching the elastic shakedown limit. After that, no further residual stresses and strains accumulate. The plastic deformation at corrugation peaks weakens the corrugation amplitude, serving as an early corrugation attenuation mechanism. Conversely, work-hardening at corrugation peaks increases wear resistance at those peaks, promoting corrugation in the long term. The explanation of the corrugation development process under the interplays of the plastic deformation and wear has been validated by field corrugation data. Additionally, we propose a wear coefficient in the wear model to account for the work-hardening and change in the wear resistance. Experimental results of the hardness distribution show the similar characteristics to the numerical results.

1. Introduction

Rail corrugation has been an important concern to both infra managers and researchers for more than one century. Rail corrugation is usually understood by wavelength-fixing mechanism and damage mechanism [1]. Many contributions from previous extensive research as reviewed in [1–4] are acknowledged in understanding most types of corrugations, yet the formation mechanism of short pitch corrugation remains elusive. Therefore, the focus of this paper is on the short pitch corrugation. This kind of corrugation is usually formed on straight tracks or at gentle curves. Its wavelength ranges from 20 mm to 80 mm [1]. Short pitch rail corrugation (hereinafter referred to as corrugation) brings many negative problems such as severe wheel-rail vibrations, system components degradation, rolling noise, and rolling contact fatigues [1]. So far, the most reliable solution is grinding [5]. However, the grinding maintenance increases the operation cost of the railway industry and reduces the network efficiency. It is, therefore, necessary to gain a concrete understanding of the corrugation development

mechanism. Concerning the research in corrugation, there are three main problems unclear or to be solved.

Firstly, the wavelength-fixing mechanism for the corrugation is usually attributed to being correlated with the pinned–pinned resonance based on that its frequency matches with the corrugation frequency [1,6]. However, the whole corrugation initiation and growth process from a smooth rail is not explicitly revealed based on the explanation. The occurrence of the corrugation in the continuous support railway track [4,7] indicates that the pinned–pinned resonance may at least, not be the only mechanism responsible for the corrugation. In addition, it is pointed out by some researchers that the pinned–pinned resonance cannot agree with field observed corrugation frequency [8]. Therefore, the wavelength-fixing mechanism is yet a problem to be elaborated on.

Secondly, the corrugation problem is usually explored with frequency-domain [6,9,10] or time-domain [11,12] models. The Analysis in the frequency domain is based on the linearization of the vehicle, track, and wheel-rail contact, and it is limited to investigation of the corrugation initial development stage [3]. However, the vehicle-track

system is a highly nonlinear system in structure and especially in the wheel-rail contact [13]. In addition, for the corrugation study, the non-Hertzian and non-steady treatment of the vehicle-track interaction process is considered as being necessary [14,15]. In this sense, time-domain models can better manifest the system and the development process. However, controversial conclusions are usually obtained with different models. Some models predicted the corrugation growth [13] but those with the non-Hertzian and non-steady treatment of the vehicle-track system [15], as proposed being necessary, reveal no corrugation growth.

Thirdly, besides the damage mechanism of differential wear, plastic deformation is usually considered as the other damage mechanism [1]. The rail material experiences dynamic loads from repeated wheel passages. When the maximum stresses are below the rail material elastic shakedown limit, the material remains elastic. However, when the stresses exceed the shakedown limit, the material will deform plastically. When the loads are removed, residual stresses arise to protect the material from further being undergone plastic deformations. This process is explained as working-hardening. When the vehicle rolls over a corrugated railway track, dynamic contact forces are excited. The periodic variation in the wheel loads makes the rail correspondingly deform periodically. This is the explanation of the damage mechanism of the corrugation in the form of plastic deformation. It means that when the corrugation severity reaches a certain stage, the non-steady effect due to the wavy profile is not negligible. The material mechanical property or structural change due to corrugation should be considered. The surface analysis of a corrugated rail material [16–18] shows that corrugation peaks experience higher plastic deformation and work-hardening, and thus have higher wear resistance, e.g., the wear resistance at corrugation peaks is twice as high as that at corrugation troughs [18]. At corrugation troughs, there is no evidence of plastic deformation caused by the large normal contact forces [16]. This agrees with the conclusion in [8] that plastic deformation cannot be active in the deepening of the corrugation trough but instead by slip and wear. Differently, Carson and Johnson [19] used a test rig to reproduce the corrugation and explained its generation as plastic deformation. Liu et al [20] experimentally studied the corrugation with a scaled test rig and observed that the corrugation trough showed a high hardness level. This indicates that corrugation development is also explained by plastic deformation. The two different roles of plastic deformation in corrugation development could be explained as two different corrugation formation mechanisms. In this sense, the research subject in the present paper is similar to the corrugation described in former paper [30,31]:1) the corrugation is shown with shiny peaks and dark valleys; 2) the dark valleys are reported as being formed due to the adhesive wear and have a rougher surface and lower hardness level [16,21]; 3) higher hardness level and wear resistance are found at the corrugation peaks [16].

Most of the previous research was focused on the investigation of the damage mechanism in the form of differential wear, with few of them dealing with plastic deformation [22–24]. Böhmer and Klimpel [22] are among the earliest researchers to consider the plastic deformation influence on corrugation and concluded that plastic deformation acts as a possible saturation mechanism on corrugation growth. With a 2D FE model, Wen et al [23] studied the corrugation initiation after a scratch on a curved rail due to plastic deformation and found that after a few load cycles the undulatory rail surface development reaches a stabilized stage. The residual stresses and strains increase at a reduced rate with increasing wheelset passages and stabilize after a limited number of wheelset passages. In [24], Wen et al extended the analysis to 3D wheel-rail rolling contact. The multiple wheel passages are simulated by multiple translations of the normal pressures and tangential tractions calculated by Kalker's exact 3D rolling contact theory. The dynamic coupling between the contact mechanics and structural dynamics is not considered in the research. The modelling of the system in continua and the interplays of the structural dynamics and the contact mechanics have been addressed in [28]. Zhao and Li [25] employed a 3D FE wheel-

rail contact model with a bilinear elasto-plastic material model of isotropic hardening and analyzed the contact solutions. Naeimi et al [26] proposed a novel method to realize the thermo-mechanical coupling with a 3D dynamic FE vehicle-track model. Solutions from different material models are compared. Wei et al [27] used a similar 3D FE dynamic vehicle-track coupled model to study the degradation in the railway crossing with considering the plastic deformation and work-hardening. However, the rail material behaviours in elasto-plasticity under cyclic wheel loads with an integrated direct vehicle-track dynamic coupled model have not yet been investigated.

Motivated by the first two problems, the current authors employed a 3D dynamic FE vehicle-track frictional rolling contact model to study corrugation development [29,30]. Some new insights are gained concerning the corrugation initiation and wavelength-fixing mechanism. Recently, Li [31] proposed a novel explanation for the corrugation initiation and consistent growth mechanism that the rail longitudinal dynamics are dominant to the corrugation initiation while the consistency of longitudinal and vertical contact forces, differential wear, and corrugation should determine the development of short pitch corrugation. The wavelength-fixing mechanism is governed by a frequency-selection explanation that the dominant frequency component could shift from a lower order to a higher order with speed increase and in the end the corrugation wavelength does not change too much. The damage mechanism of the corrugation considered is differential wear, as generally attributed to be the main damage mechanism [1–8]. Consequently, a corrugation mitigation method was investigated [32]. In this paper, the third problem clarified above that the plastic deformation as another damage mechanism of corrugation, will be investigated with the proposed method in this paper.

Main goals of this research are: 1) to propose a numerical method which can deal with the material responses under cyclic axle loads, with which the material residual stresses/strains can be considered. 2) to investigate the response of rail material to short pitch corrugation by cyclic axle loads and analyse the influence of plastic deformation on the development of short pitch corrugation. 3) to examine methods for integrating the effects of material work-hardening into the wear model. 4) to gain evidence from the experimental tests and observations for checking of the numerical results. To this end, the structure of the paper is organized as follows. Section 2 presents the numerical model with a dynamic three-dimension (3D) finite element (FE) vehicle-track frictional rolling contact model, and the method of cyclic wheel-rail interactions. Section 3 discusses the modelling of the fastening system for which an initial excitation is introduced in the model and with which the corrugation can initiate and grow consistently. The corrugation model used in the current investigation will be based on this corrugation. Section 4 shows the results of the investigations. Section 5 presents some experimental results and based on the above analysis a wear model which needs to consider the rail material work-hardening effects is proposed. The postulation of the corrugation development under the interplay of wear and plastic deformation is further analyzed. Finally, some conclusions are summarized in the last section.

2. Model and method

2.1. The 3D FE vehicle-track model

A 3D dynamic FE vehicle-track coupled frictional rolling contact model used in [30] is employed in this paper to include the elasto-plasticity material property and the influence of multiple wheel passages, i.e., the accumulation of residual stresses and strains from cyclic axle loads. The model is developed with Ansys/Ls-Dyna. It considers a corrugation situation on straight tracks. Hence, the vehicle-track model is treated as being symmetrical about the track center and a half wheelset and track structure are modelled. The structure above the primary suspension is lumped as mass elements as their vibration frequency is usually not higher than 10 Hz [33], in comparison with the

corrugation frequency of 500–2000 Hz (corresponding to 20–80 mm corrugation wavelength under typical Dutch train speed of 140 km/h). The wheelset, rail, and sleepers are modelled as 3D solid elements. The rail is UIC 54 E1 with a nominal profile. The wheel geometry was that of the ICR car, with nominal wheel radius of 0.46 m, and 1/40 conicity to match the rail inclination of the same value. The sleeper in the model considers the monoblock concrete sleeper [34]. The sleeper spacing is the nominal value of 0.6 m. The primary suspension, fastening system (usually represented by railpad), and ballast are modelled with spring-damper elements. A linear elastic spring and a linear viscous damper are considered with parameters in Table 1. A dynamic factor of 30% is designed and applied in the static sprung load to consider the dynamic load in low frequencies and the non-uniform distribution of car-body weight on the different wheels [35]. The sprung load with consideration of the dynamic factor is 93 kN. Other parameters are from the typical Dutch track system [21,30].

The wheel and rail are meshed with 8-node solid elements. In the solution zone marked in Fig. 1, the mesh size in the contact surface is 0.8 mm × 0.8 mm to guarantee a high solution accuracy [38]. The total number of elements in the model is 1,169,760, and the number of nodes is 1,346,380. The CPU time of each wheel passage cycle is about 12.5 h. The simulations were performed on a workstation with Intel(R) Xeon(R) Gold 6244 @ 3.60 GHz 16 cores CPU and 256 GB RAM. Additionally, a High Performance Computation (HPC) module with 13 processors is used. The contact between wheel and rail is modelled with a surface-to-surface contact algorithm based on a penalty method [36]. This penalty algorithm applies a penalty function to the contact forces to enforce the contact constraints and solve the penetration problem between contact bodies. The penalty contact algorithm can be straightforwardly implemented in the explicit FE programs as a subroutine [37]. Coulomb's frictional law is used with a friction coefficient of 0.4 [31]. A traction coefficient of 0.15, defined as the ratio between longitudinal tangential load and the normal load, is employed to generate an adhesion-slip wheel-rail contact situation. The validity of the model in statics and dynamics has been validated by comparing the FE results with results from other established methods [38,39], with impact hammer tests [40] and ABA measurements [41]. An explicit time integration scheme is employed to consider the transient wheel-rail fictionally rolling contact. Courant stability condition [42] should be fulfilled to ensure the convergence, i.e., the time step is small enough so that the sound wave may not cross the smallest element within one-time step. As long as the time step is sufficiently small, all relevant vibration modes of the structure and the continua will be automatically included in the solution. In addition, the contact mechanics and the vehicle-track system structural dynamics are instantaneously coupled. This renders the model to consider their mutual influence, and it is important for high-frequency dynamic interactions. In the 3D FE vehicle-track model, the nonlinearity in contact mechanics, structural dynamics, and complex materials models can all be considered. The rail grade considered is

Table 1
Vehicle parameters and Track parameters.

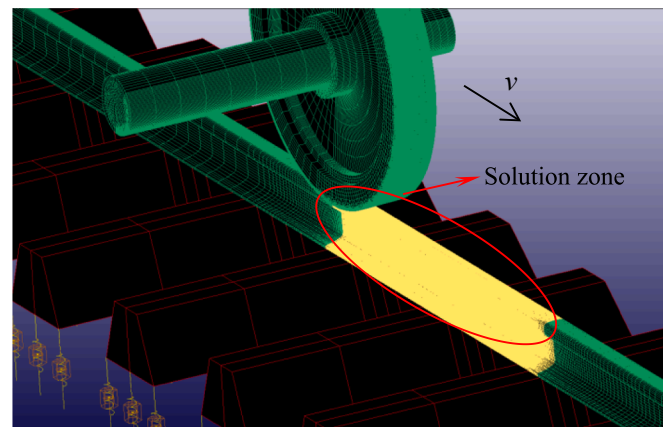| Parameters		Values
Primary suspension	Stiffness	1.15 MN/m
	Damping	2.5 kNs/m
Railpad	Stiffness	1,300 MN/m
	Damping	45 kNs/m
Ballast	Stiffness	45 MN/m
	Damping	32 kNs/m
Wheel and rail material	Young's modulus	210 GPa
	Poisson's ratio	0.3
	Density	7,800 kg/m^3
	Tangent modulus	21 GPa
	Yield strength	500 MPa
Sleeper	Young's modulus	38.4 GPa
	Poisson's ratio	0.2
	Mass density	2520 kg/m^3

Fig. 1. 3D FE vehicle-track model.

R260 Mn. To include the work-hardening of plastic deformation, a bi-linear plastic material model with kinematic isotropic hardening is used. The yield strength of the rail and wheel is $\sigma_y = 500$ MPa [25,43]. The hardening curve, represented by the tangent modulus, is $G = 21$ GPa [25,43].

2.2. Simulation of vehicle-track contact with multiple wheel passages

The numerical simulation follows an implicit-to-explicit procedure. In the implicit, it calculates the initial stresses and strains of a wheel sitting on the rail. This analysis defines the initial state of the dynamic analysis when stress initialization is performed in the explicit integration method. By doing it, the unrealistic vibration that may be caused by in-equilibrium state of the system can be avoided. Then, in the explicit, the wheel is set to roll on the rail together with dynamic relaxation. The dynamic relaxation process damps out the initial imbalance due to the imperfect static equilibrium. An initial distance of 0.3 m is given to guarantee a sufficient dynamic relaxation process. The solution zone is in the range of 0.3 m ∼ 0.9 m.

The rail material behaviour with a direct integrated vehicle-track coupled dynamic interaction under cyclic wheel loads is deserved to be studied to consider the role of plastic deformation on corrugation development. The approach for simulating multiple wheel passages considering the cyclic plastic deformation accumulation is illustrated in Fig. 2. In step 1, the wheel starts from the original stationary location to roll along the rail for cycle 1 without initial stresses and strains in the solution zone. At the end of cycle 1 in step 2, residual stresses, and strains from cycle 1 are automatically saved. In step 3, the wheel starts to roll from the same initial location along the rail. The rail material was updated to include the residual stresses and strains from the first cycle. When the wheel rolls over the solution zone, the residual stresses, and strains from cycle 2 accumulate and the residual stresses and strains in step 4 are updated, recorded, and will be included in the following cycles. The updating of the residual stress is shown in Fig. 3 more explicitly.

2.3. Von Mises stress and effective plastic strain

The Von Mises yield criterion, also known as the maximum distortion energy criterion, is a widely used theory for predicting the plastic deformation in ductile materials. According to this criterion, yielding occurs when the Von Mises stress reaches a critical value that depends on the yield strength of the material. The Von Mises stress is a measure of the distortion energy of a material and is based on the three principal stresses that act on a material. Once the yield strength is exceeded, plastic deformation occurs in the material, which causes residual stress. The Von Mises stress can be expressed mathematically as [44]
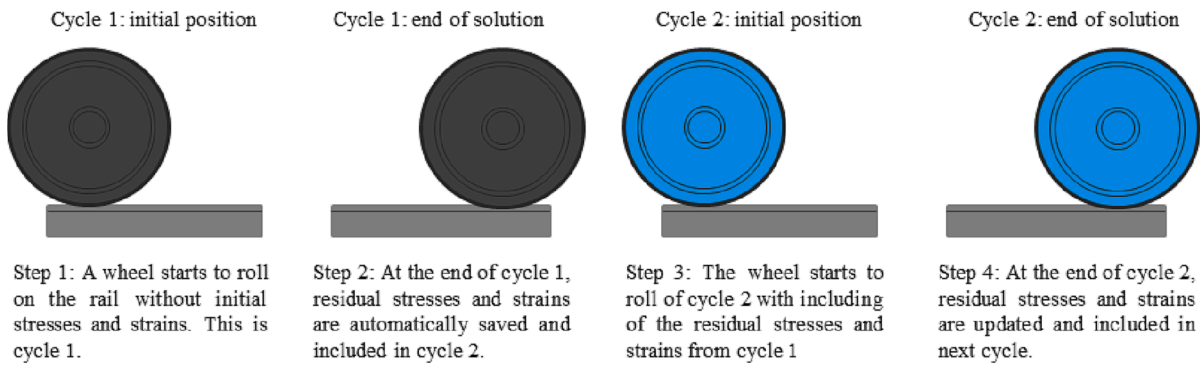
Cycle 1: initial position   Cycle 1: end of solution   Cycle 2: initial position   Cycle 2: end of solution

Step 1: A wheel starts to roll on the rail without initial stresses and strains. This is cycle 1.

Step 2: At the end of cycle 1, residual stresses and strains are automatically saved and included in cycle 2.

Step 3: The wheel starts to roll of cycle 2 with including of the residual stresses and strains from cycle 1

Step 4: At the end of cycle 2, residual stresses and strains are updated and included in next cycle.

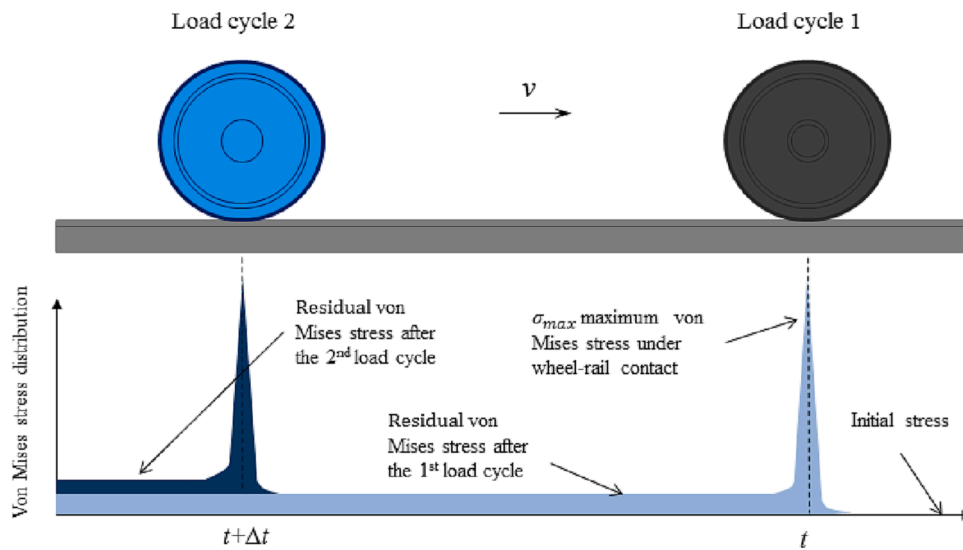**Fig. 2.** Multiple steps for simulating cyclic wheel passages.

Fig. 3. Schematic of updating stresses in the numerical process of the cyclic wheel passages.

$$\sigma_v = \sqrt{\frac{1}{2}\left[\left(\sigma_{xx} - \sigma_{yy}\right)^2 + \left(\sigma_{yy} - \sigma_{zz}\right)^2 + \left(\sigma_{zz} - \sigma_{xx}\right)^2 + 6\left(\sigma_{xy}^2 + \sigma_{yz}^2 + \sigma_{zx}^2\right)\right]} \tag{1}$$

where σ_{xx}, σ_{yy} and σ_{zz} are the normal stresses; and σ_{xy}, σ_{yz} and σ_{zx} are the shear traction.

Effective plastic strain characterizes intensity of plastic strains. It is a monotonically increasing scalar value which is calculated from the components of plastic strain rate tensor as [45,46]

$$\varepsilon_p = \int_0^t \dot{\varepsilon}_p dt \tag{2}$$

$$\dot{\varepsilon}_p = \frac{\sqrt{2}}{3}\sqrt{\left(\dot{\varepsilon}_{px} - \dot{\varepsilon}_{py}\right)^2 + \left(\dot{\varepsilon}_{py} - \dot{\varepsilon}_{pz}\right)^2 + \left(\dot{\varepsilon}_{pz} - \dot{\varepsilon}_{px}\right)^2 + 6\dot{\varepsilon}_{pxy}^2 + 6\dot{\varepsilon}_{pyz}^2 + 6\dot{\varepsilon}_{pzx}^2} \tag{3}$$

where ε_p is the plastic strain tensor, $\dot{\varepsilon}_p$ is the plastic strain rate tensor, and $\dot{\varepsilon}_{px}$, $\dot{\varepsilon}_{py}$, $\dot{\varepsilon}_{pz}$, $\dot{\varepsilon}_{pxy}$, $\dot{\varepsilon}_{pyz}$, $\dot{\varepsilon}_{pzx}$ are the 6 components of the deviatoric part of the plastic strain rate tensor for isotropic elasto-plastic material.

3. The corrugation model

3.1. Fastening system modelling

In [31], we proposed a concept of initial excitation. With this initial excitation, the wheel-rail dynamic contact is excited and differential wear is produced. The initial excitation was introduced with the
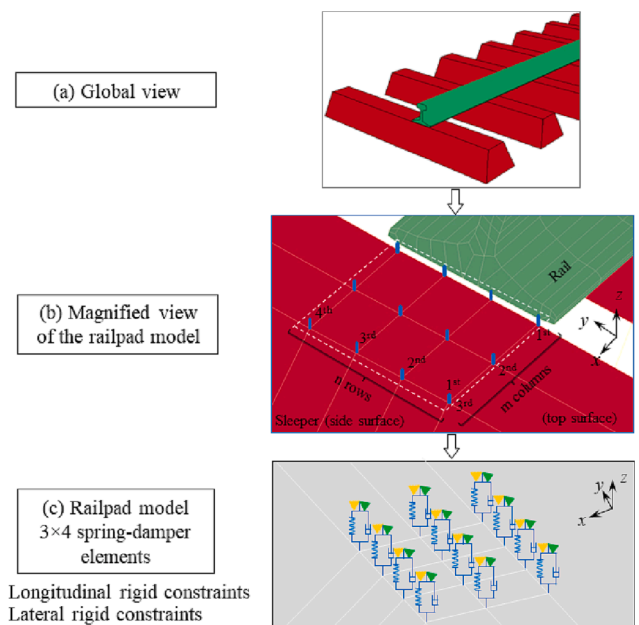

(a) Global view

(b) Magnified view of the railpad model

(c) Railpad model 3×4 spring-damper elements

▼ Longitudinal rigid constraints
▼ Lateral rigid constraints

Fig. 4. Fastening model for corrugation consistent initiation and growth.

variation of rail fastening modelling as shown in Fig. 4. The fastening is represented with 4×3 columns and rows of spring-damper elements and constrains the rail in the longitudinal (*x*), lateral (*y*), and vertical (*z*) directions. It was found that when the longitudinal constraints in the first and third columns at the rail foot were released, the initial excitation was produced. Consequently, large fluctuations of wheel-rail longitudinal contact forces and different wear are observed (see Fig. 5). Further, it is noted that there is a close correlation between the longitudinal contact force and the differential wear.

3.2. Consistent corrugation initiation and growth

The large fluctuation of differential wear is the perquisite for corrugation initiation according to the initial damage mechanism of wear. Next, the corrugation formed by the differential wear is found being capable to consistently grow. The definition of the term "consistent" means that the differential wears calculated with and without corrugation are the same in wavelength and phase angle which guarantees the differential wears from multiple wheel passages can accumulate. This process can be explicitly shown in Fig. 6. The first sub-figure (upper) shows the differential wear calculated when the rail is smooth which we name it as the initial differential wear. The fourth (lower) sub-figure shows the applied corrugation in the model which is in anti-phase with the differential wear in the first subfigure. The corrugation maximum peak-to-trough amplitudes ($2A_{max}$) are varying from 10 μm to 40 μm, 80 μm and 160 μm. It can be observed that when $2A_{max} \leq 80$ μm, the calculated differential wears with corrugation are generally consistent with the initial differential wear but with a decreasing amplitude, while when $2A_{max} = 160$ μm, the different wear is in anti-phase with the initial differential wear. When they are consistent,

it means the corrugation can further grow, otherwise the corrugation will be levelled out. With the study, the whole corrugation development process from initiation, growth and saturation is successfully reproduced.

3.3. Corrugation model

In previous research, the applied corrugation in the model is usually artificially designed. There are several disadvantages. Firstly, the used model could well represent a healthy condition which means the corrugation does not necessarily be formed. Secondly, the artificially applied corrugation may disagree with the model determined corrugation in wave pattern. Thirdly, with above issues wrong conclusions could be derived. To avoid such problems, the corrugation input to the model is based on the above calculations in section 3.2. A further benefit it brings with this method is that interplay of the differential wear and plastic deformation during the corrugation growth can be investigated.

To this end, the corrugation applied in the FE model is the same as in Fig. 6. As shown in Fig. 7a, the corrugation wavelength and amplitude are not constant. This typical corrugation pattern resembles a corrugation example observed on the Dutch railway network (see Fig. 7b).

To investigate the influence of different corrugation severities on plastic deformation, different amplitudes of the corrugation are considered. Therefore, a parameter $2A_{max}$ as shown in Fig. 5b is introduced and varies from 0 μm to 10 μm, 50 μm, 100 μm, and 200 μm. By attributing the 200 μm amplitude, we expect to consider a critical corrugation situation.

(a)　Differential wear and contact forces in spatial domain

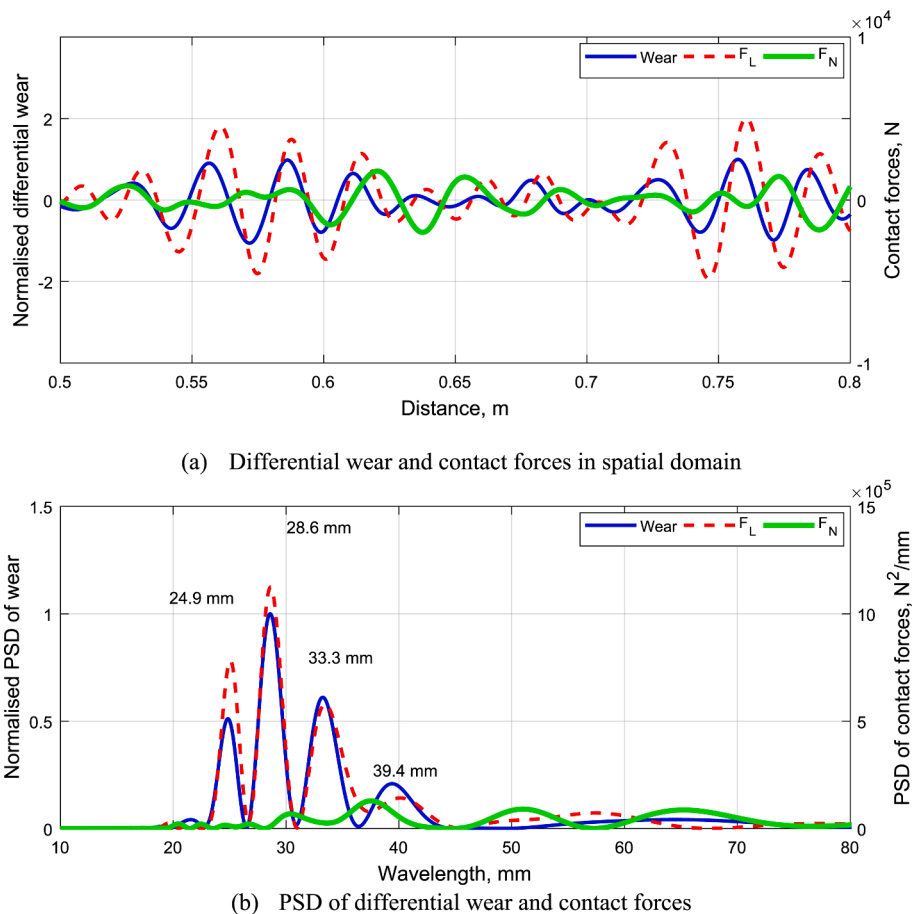(b)　PSD of differential wear and contact forces

Fig. 5. Fluctuations of wheel rail contact force and differential wear (F_L: longitudinal contract force, F_N: vertical contact force, PSD: power spectral density) [31].
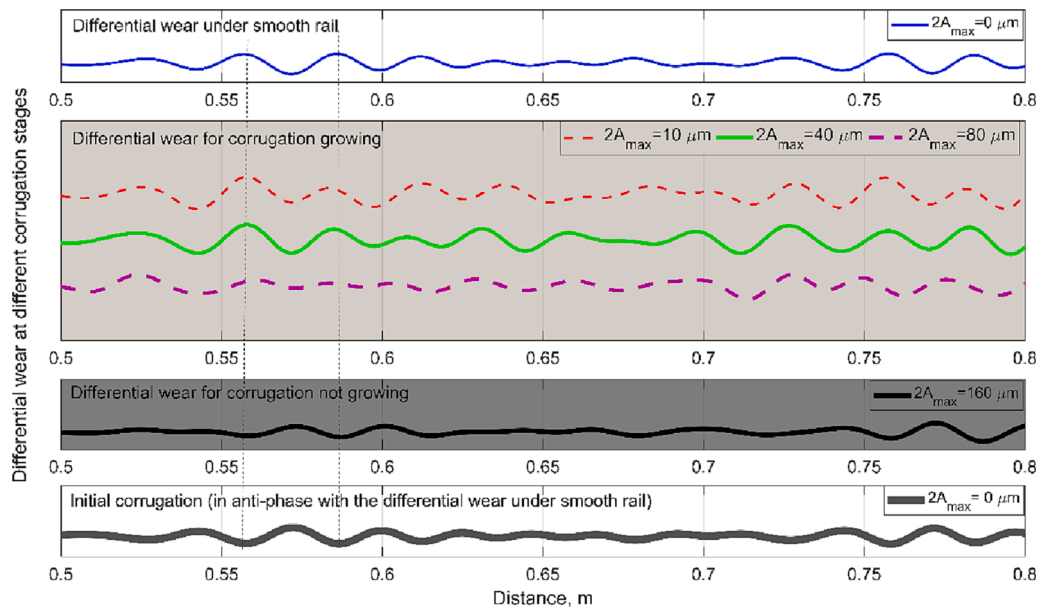
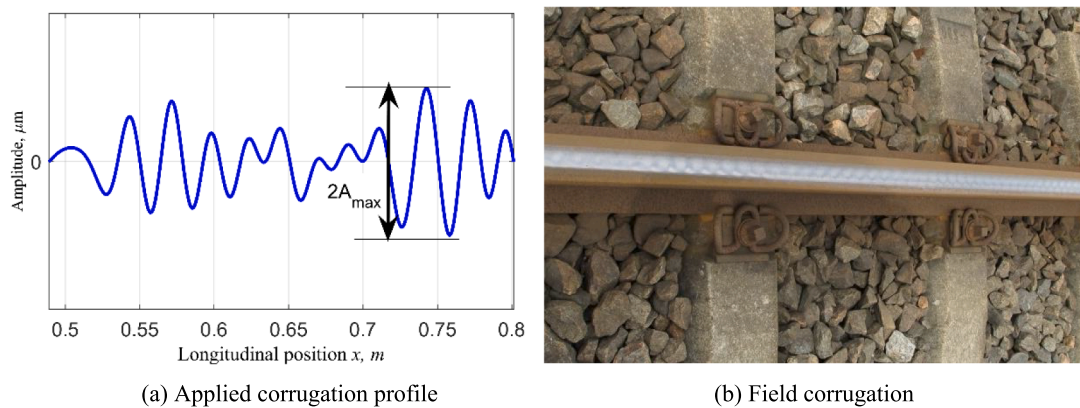Fig. 6. Consistent corrugation initiation and growth [31].

(a) Applied corrugation profile

(b) Field corrugation

Fig. 7. Corrugation profile applied in the model.

4. Results and analysis

4.1. Comparison of the von Mises stress and effective strain with and without corrugation

Fig. 8 shows the comparison of the residual stresses and the effective plastic strain (EPS) under the smooth rail and corrugated rail situations. The amplitude considered in this case is $2A_{max} = 200$ μm. As shown in Fig. 8a, the maximum residual stress lies beneath the rail surface, indicating a large von Mises (V-M) stress history in the same depth. The influence of the friction and traction coefficients on the maximum V-M stress distribution along the depth has been studied in [28], therefore the phenomenon that maximum V-M stress is in the subsurface can be well understood from the current parameters. In addition, the distribution of the residual stress tends to be regular when the rail is smooth. In the presence of the corrugation, the residual stress intensity redistributes and keeps in–phase with the applied corrugation (see Fig. 9a), i.e., corrugation peak with a higher residual stress level. The same phenomenon applies to the EPS as shown in Fig. 8b and Fig. 9b, respectively.

To reveal the difference in the maximum V-M stress at the corrugation peak and corrugation trough, the maximum V-M stress along the depth under the smooth rail and corrugated rail situations are obtained and shown in Fig. 10. Under the smooth rail condition, the maximum V-M stresses at two positions are not the same. This is due to the transient vehicle-track interactions. With corrugation, the overall V-M stress level at the corrugation peak increases considerably above the yield stress of 500 MPa. At the corrugation trough, the V-M stress, however, drops significantly with the maximum value of less than 300 MPa.

4.2. Influence of the corrugation amplitude on V-M stress and EPS

Figs. 11 and 12 show the V-M stresses and EPS under different corrugation severities with the amplitudes $2A_{max}$ varying from 0 μm to 200 μm. with the increase of the corrugation amplitudes, the V-M stresses and strains increase correspondingly at the element of 682718, which is an element at the rail surface and the corrugation peak. Inversely, the V-M stresses and strains decrease continuously with the corrugation amplitude increase at a corrugation trough element. The large V-M stresses will cause plastic deformation and lead to two effects: 1) the reduction in the corrugation peak which acts as a corrugation attenuation mechanism as mentioned in [22]; 2) the work-hardening at the corrugation peak to increase the wear resistance. At the corrugation trough, however, due to the lower V-M stress than the yield stress, the plastic deformation cannot be active. That means the main damage at
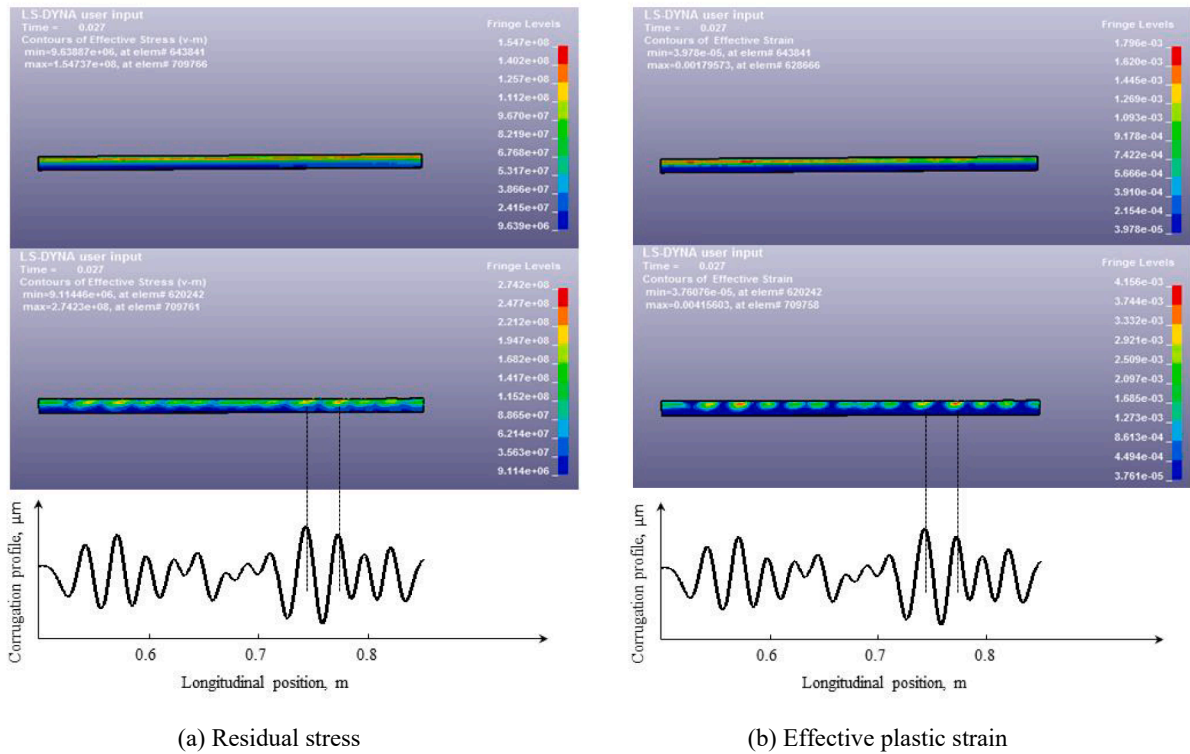
(a) Residual stress

(b) Effective plastic strain

Fig. 8. Comparison of residual stress and effective plastic strain under a smooth rail and under corrugation situation ($2A_{max}$ = 200 μm).

(a) Residual von Mises stress
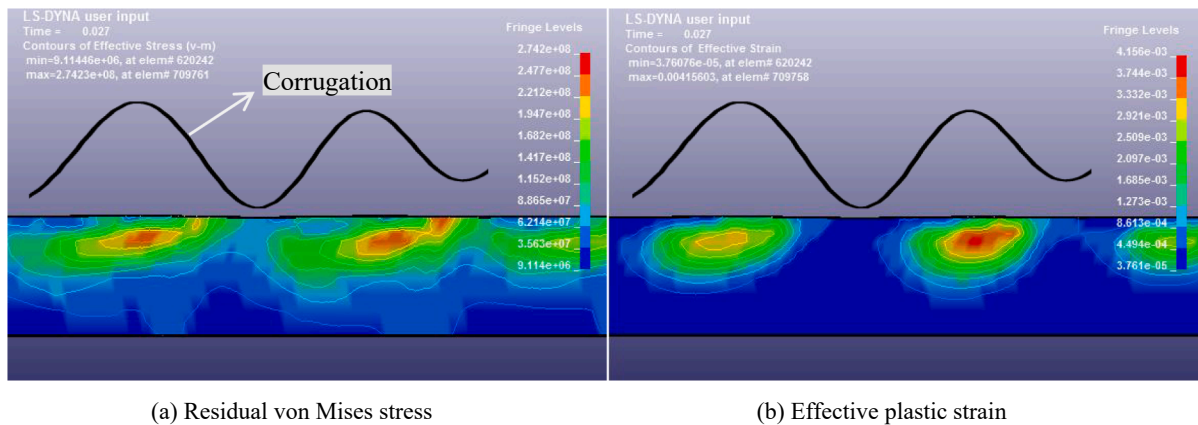
(b) Effective plastic strain

Fig. 9. Magnification to reveal the localized residual stress and effective plastic strain.

the corrugation trough is reasonable to be considered as differential wear.

4.3. V-M Stress and EPS under multiple wheel passages

The cyclic plastic deformation and work-hardening of the element 682,718 at the corrugation peak under multiple wheel passages are shown in Fig. 13. The V-M stress after 2 load cycles drops down below the initial yield stress of 500 MPa. It means the material at element 682,718 enters elastic shakedown. In cycle 3, no further EPS is observed. In [23], it is reported that the EPS increases at a decreasing rate. The same phenomenon is observed that the EPS in cycle 2 is smaller than that in cycle 1. It is necessary to mention that for other elements, the number of cycles to reach the elastic shakedown process varies from 3 ~ 5. In summary, the rail material will show an elastic shakedown behaviour after limited loading cycles.

The stress–strain behaviour of the materials in the multiple cycles is

shown in Fig. 14. Looking at element 682718, the total strain is about 3.8×10^{-3} in cycle 1, leaving with about 1.5×10^{-3} EPS after removing the load. The yield stress after the first cycle increases from 500 MPa to 530.8 MPa. In the second cycle, the EPS is 0.46×10^{-3}. The total accumulation of EPS is 1.96×10^{-3}. The yield stress after 2 load cycles becomes 538.2 MPa. In cycle 3, the rail material is purely elastic, and there is no further plastic deformation accumulated nor increase in the yield stress. At the other element of 701723, the number of load cycles for the rail material to reach the elastic shakedown limit is 4.

5. Experimental characterization of corrugated rail materials

5.1. Hardness distribution in phase with corrugation

Some rail samples with corrugation wave patterns are taken for the experimental studies as shown in Fig. 15. The first corrugation shows a corrugation situation with varying amplitude. The second corrugation
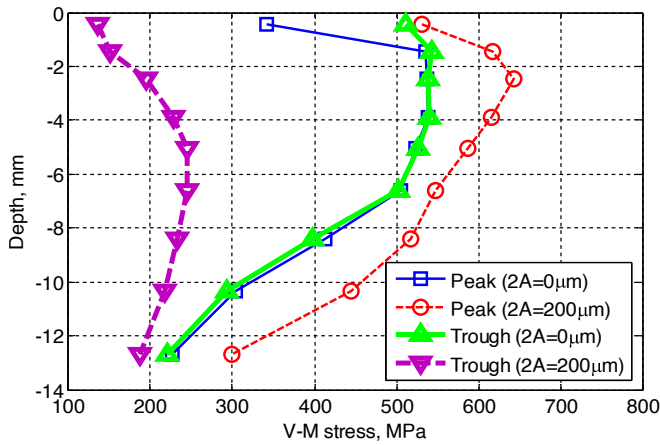
Fig. 10. The maximum V-M stress distribution in rail depth at corrugation peak and trough under $2A_{max} = 0$ and 200 µm respectively (Element 682,718 corresponds to corrugation peak, and element 682,700 corresponds to corrugation trough).

illustrates a roughly equal distribution of the corrugation in wavelength but with some shorter sub-wavelengths (see Fig. 15b). The profile of the second corrugation is measured with a laser-based 3D HandyScan, from which the rail surface roughness can be obtained.

Fig. 16a shows one section corrugation profile in the longitudinal extracted from 3D scanning geometry data. To better reveal the corrugation, two different band-pass filterings (BPF) schemes are applied to the data, one with BPF of 20–80 mm (the typical corrugation wavelength range), and the other with 5–80 mm (considering the sub-wavelengths shorter than 20 mm). By comparing the rail surface appearance of dark (corrugation trough) and bright (corrugation peak) running band,

the measurement can well represent the geometry variation. The shorter sub-wavelengths in the corrugation visually observed can also be identified with the measurement.

It is reported that corrugation peaks experience high wheel-rail contact forces and therefore become harder due to the working-hardening effect [22]. To reveal it, a hardness test is performed with a GE DynaMIC hardness tester. The distribution of the hardness is synchronized with the profile measurement in the spatial domain. As shown in Fig. 16b, the higher hardness peaks correspond to corrugation peaks. The highest hardness at those peaks can be larger than 350 Hv. Thus, the corrugation peaks have a hardness level of 30–100 Hv higher than that at corrugation troughs. The result is in agreement with the previous findings in [47]. Note that at 100 mm, the profile trough corresponds to a small rail defect. The higher hardness values at the trough could be due to the defect-induced high impact loads.

5.2. Microstructural characterization

In the presence of corrugation, there are impact vibrations between the wheel and rail. Therefore, the rail material along the corrugation experiences different degrees of damage under the dynamic contact loads, and the material microstructural features, i.e., the topographic features, or phase transformations, along a corrugation wave also vary periodically. Much research [22,30] reveals that the dynamic contact forces are in-phase with the corrugation and hence rail surface materials at the corrugation peaks show severer structural damages, e.g., the occurrence of white etching layer (WEL) [16–18,47]. The WEL is very brittle and its hardness of it can be up to 1200 Hv. Due to the higher hardness, the layer is highly in wear resistance. According to [17], the wear resistance of the material at the corrugation peak can be twice that at the corrugation trough.

In this study, the rail material from corrugation one is characterized.
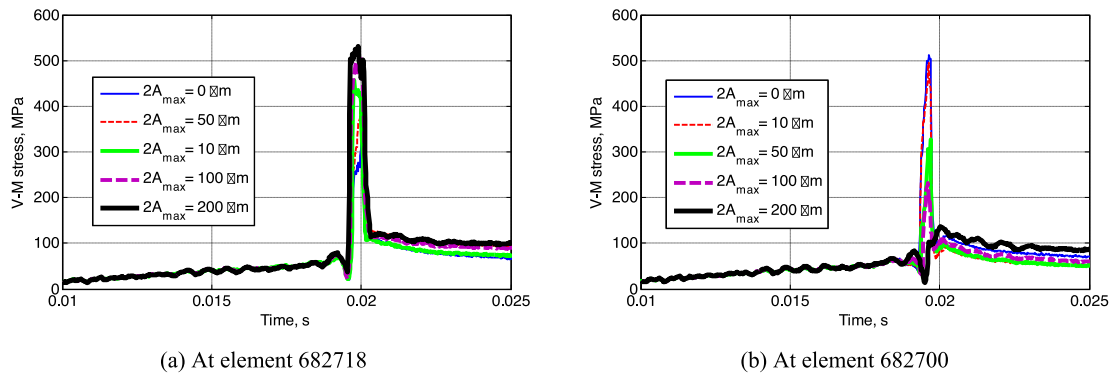

(a) At element 682718

(b) At element 682700

Fig. 11. Von Mises stress distribution of the surface elements at corrugation peak and trough under different corrugation amplitudes.
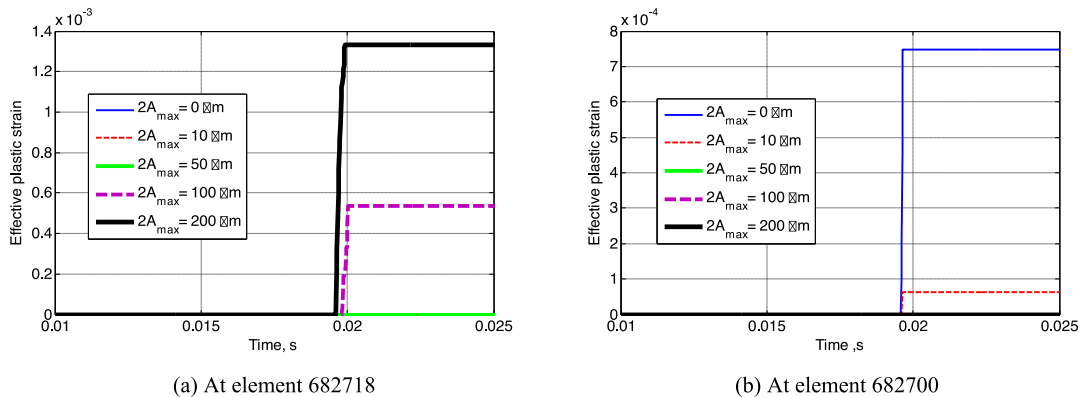

(a) At element 682718

(b) At element 682700

Fig. 12. Effective plastic strains distribution of the surface elements at corrugation peak and trough under different corrugation amplitudes.
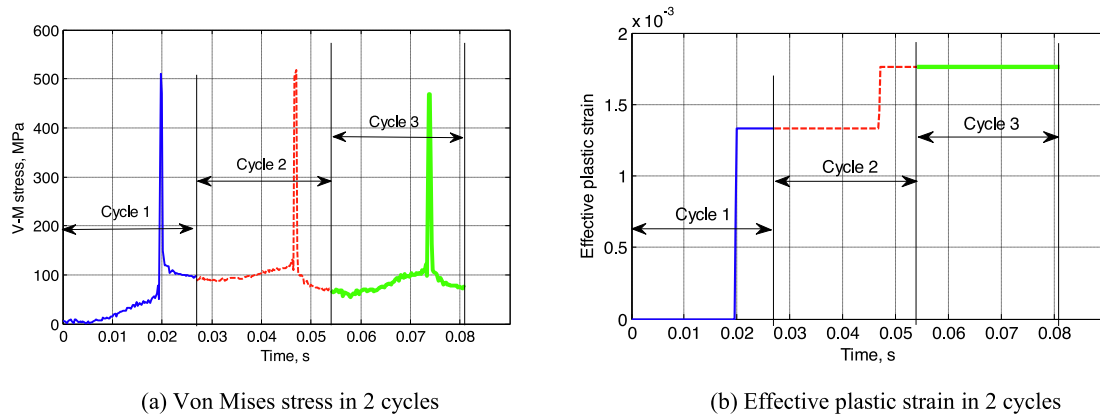
(a) Von Mises stress in 2 cycles

(b) Effective plastic strain in 2 cycles

Fig. 13. The cyclic plastic deformation and work-hardening at the element of 682718.

(a) At element 682718

(b) At element 701723
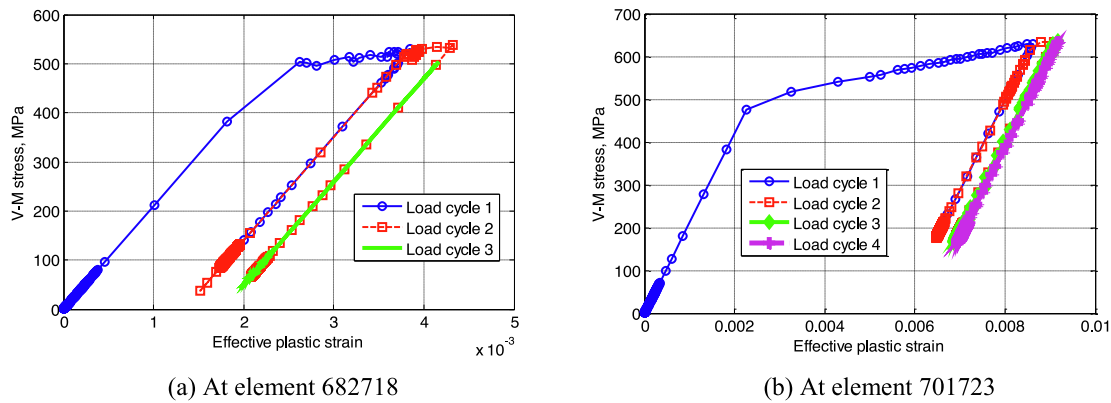
Fig. 14. V-M stress and EPS under limited load cycles at 2 elements.

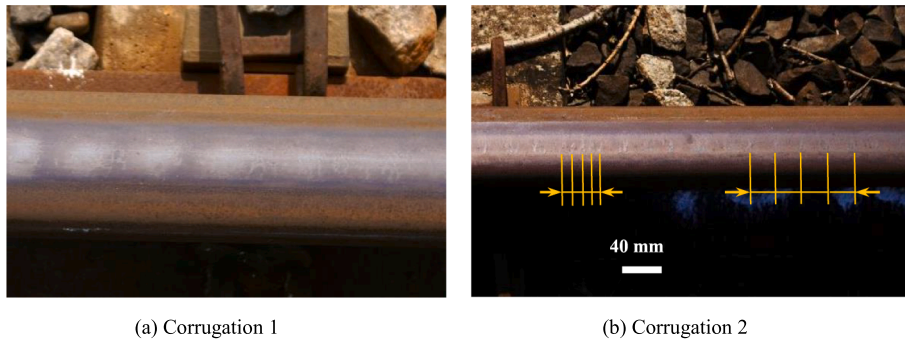(a) Corrugation 1

(b) Corrugation 2

Fig. 15. Two corrugation examples referred in this research.

The specimens are sectioned along the longitudinal-vertical direction. It is prepared with a standard metallurgical procedure and finally etched in a 3 vol% solution of HNO3 in ethanol (Nital). The microstructural features at the corrugation peak and trough are shown in Fig. 17. WEL and brown etching layer (BEL) are observed at the corrugation peak, while not at the corrugation trough. The microhardness test undertaken in [47] indicates that the hardness for the WEL can be 882.7 ± 63.3 HV, and 450–470 HV for BEL. Therefore, during the corrugation development, the material structural change at corrugation peaks brings much difference in the wear resistance [16,17]. This difference in wear resistance is significant for studying the long-term corrugation development due to the differential wear. In the next section, rail material is treated in elasto-plasticity to consider the work-hardening due to cyclic plastic deformation.

5.3. A wear resistant coefficient introduced in the wear model

The damage mechanism of differential wear is usually assumed to be proportional to the frictional work [6,13,15]. It is expressed as

$$w(x, y) = kW_f(x, y) = k \sum_{i=1}^{N} \tau_i(x, y)v_i(x, y)\Delta t \qquad (4)$$

where k is the wear coefficient, $W_f(x, y)$ is the frictional work, $\tau_i(x, y)$ and $v_i(x, y)$ are the local tangential stress and slip, respectively, and N is the number of time steps Δt during which the element passes through the contact patch.

However, when there is a periodic work-hardening of the rail material due to the corrugation, the wear resistance should be highly periodic. In this case, the wear coefficient k should not be a constant
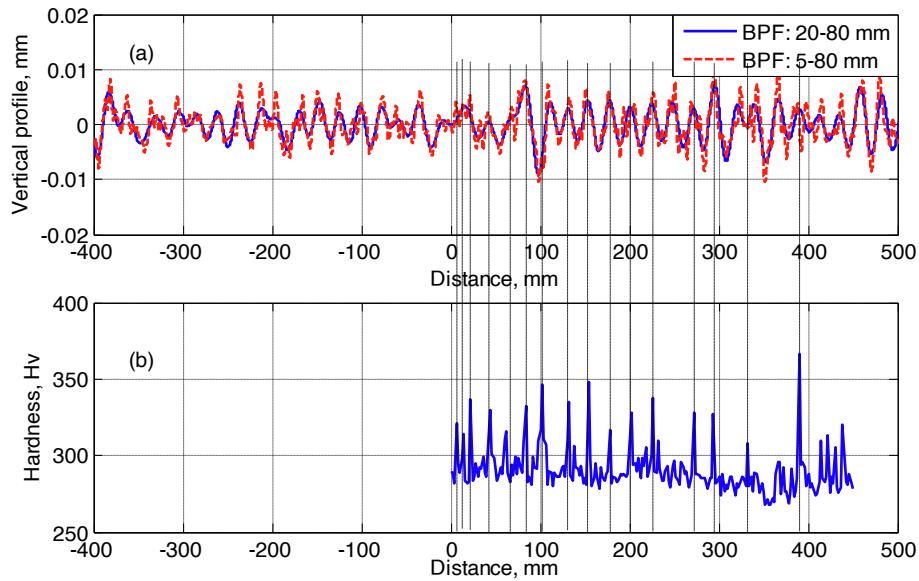
Fig. 16. Rail longitudinal-vertical corrugation profile in comparison to the hardness profile.
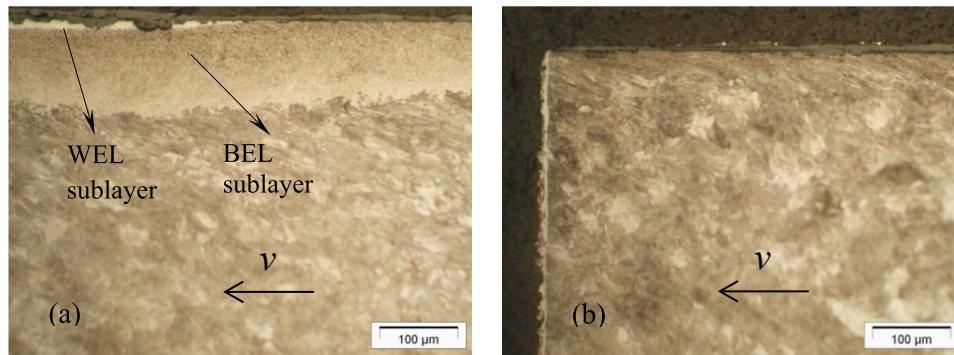

Fig. 17. Microstructural features at corrugated rail (a) peak and (b) trough.

parameter, and the wear model needs to be updated as

$$w(x,y) = kW_f(x,y) = k(x,y) \sum_{i=1}^{N} \tau_i(x,y)v_i(x,y)\Delta t \qquad (5)$$

where $k(x,y)$ is a spatial varied wear coefficient which takes into consideration of the material variations in wear resistance due to work-hardening. It is defined as

$$k(x,y) = k_0(1 + \alpha H(x,y)/H_0) \qquad (6)$$

where k_0 is the reference wear coefficient of pearlitic bulk material for R260 Mn, α is a parameter to correlate the hardness to wear coefficient, $H(x,y)$ is the spatial varying hardness calculated from $\sigma_y(x,y) = H(x,y)/3$ [48], and H_0 is a reference hardness for the rail of R260 Mn.

When taking into consideration the wear coefficient changes in the wear model, the higher wear resistance at corrugation peaks will act as a corrugation promotion mechanism that intensifies the differential wear for corrugation growth.

6. A postulation of the corrugation development mechanism under the interplays of differential wear and plastic deformation

At the corrugation initiation stage, the excited periodic contact forces due to the corrugation are small in amplitudes. The variations in contact force, periodic plastic deformation, and work-hardening are negligible. Therefore, it is reasonable to assume that the main mechanism that contributes to corrugation growth as being differential wear. When the severity of the corrugation reaches a certain stage, the periodic plastic deformation and work-hardening are more active to cause on one hand the larger plastic deformation at the corrugation peaks but not at corrugation troughs, and on the other hand the work-hardening and the increase in the wear resistance at corrugation peaks. Seen from the current results and similar results in [23,24] that the elastic shakedown limit will be reached after limited load cycles, it can be concluded that the plastic deformation at corrugation peaks which weakens the corrugation amplitude acts as the corrugation attenuation mechanism [22] in the early load cycles. Under the elastic shakedown behaviour and the higher wear resistance of the rail material at corrugation peaks, the corrugation explained based on the differential wear will be strengthened. On the other hand, the differential wear tends to decrease in amplitudes and become in-phase with the corrugation with the corrugation amplitude increase. In this sense, the plastic deformation acts as a corrugation promotion mechanism in the long term.

This proposed explanation can be understood and validated from the following two aspects regarding the influence of rail grade.

1) The study of the rail material's influence on the corrugation in the Netherlands [3,21] shows that the rail material with lower wear resistance, i.e., lower hardness level, shows less corrugation and less work hardening at the rail surface. According to the explanation of

differential wear, a higher wear rate will accelerate the corrugation growth. Therefore, the field data seems in contradiction with the previous explanation. However, when taking into consideration of the proposed explanation in the present paper that the work hardening at the corrugation peaks plays a corrugation promotion mechanism, the observed phenomenon will be easily understood. The work hardening layer due to the plastic deformation is more quickly worn off, and its positive contributions to the corrugation growth are less active in the soft rail material. In the end, the corrugation will arrive at a saturation stage earlier and with a comparably smaller corrugation amplitude. In the end, the rail surface appears smoother than the hard rail material.

2) In another research, however, the application of head hardened rail grade, e.g., R350HT, is suggested to mitigate the corrugation [49]. Field tests over 2 years show that the corrugation formed on R350HT rail was a third less than for the grade 900A (R260) [49]. This seems in contradiction with the previous field observations and in contradiction with the proposed explanation of the corrugation growth. This phenomenon is due to the fact that the quite hard rail material greatly increases the wear resistance. The corrugation due to the wear grows at a quite slow rate with a quite slowly increasing amplitude. Under such a situation, the differential plastic deformation, i.e., periodically varying with the corrugation profile, due to the impact vibrations caused by the corrugation, is also less active. Under the combination of high wear resistance and less active differential plastic deformation, the corrugation in the hard material grows slower than it in the comparably soft material.

Hence, the proposed explanation based on the interplays of differential wear and plastic deformation shows its validity in explaining the field observations of corrugation development. A further conclusion from the analysis is that the corrugation can be mitigated either by choosing much softer rail material in which the wear rate is much larger than the accumulation of work hardening material layer or by heat-treated rail material with much higher hardness and thus much higher wear resistance to reduce the wear rate and the plastic deformation. Of course, the rolling contact fatigue (RCF) problem is also a concern from the consideration of a competitive role between the wear and RCF [50]. This is from the aspect of the rail material consideration to mitigate the corrugation problem.

7. Conclusions

An integrated 3D dynamic FE vehicle-track model is developed in this research with a novel application in studying the rail corrugation in elasto-plasticity under cyclic wheel loads. The wheel and rail materials are treated as bilinear elasto-plastic with isotropic kinematic hardening. The residual stresses and strains from one load cycle are automatically recorded and included in the following load cycles to consider the accumulation phenomenon. Based on the obtained results, the main conclusions are made as follows:

1. A method is proposed to study the rail material response in elasto-plasticity under cyclic wheels loads. The method considers the direct coupling between the structural dynamics and the contact mechanics. Their interplays, i.e., the instantaneous influence on each other, can be taken into consideration.
2. The damage mechanism under the interplays of wear and plastic deformation is proposed. Its validity in the explanation of the field corrugation data is shown.
3. Some suggestions concerning choosing rail grades to mitigate corrugation are proposed based on the explanation and the field corrugation data.
4. A wear coefficient to consider the differential plastic deformation induced work hardening is proposed.

5. The limited number of cycles of entering the elastic shakedown cycles is in agreement with previous research results.

Yet the wear coefficient which considers that work-hardening is not quantified in this paper. Further research needs to be undertaken to measure the change of the rail material hardness and the profile change from which a valid relationship can be possibly derived.

Declaration of Competing Interest

The authors declare that they have no known competing financial interests or personal relationships that could have appeared to influence the work reported in this paper.

References

[1] Grassie SL. Rail corrugation: characteristics, causes, and treatments. P I Mech Eng F-J Rai 2009;223:581–96.
[2] Sato Y, Matsumoto A, Knothe K. Review on rail corrugation studies. Wear 2002; 253:130–9.
[3] Nielsen JCO, Lundén R, Johansson A, Vernersson T. Train-Track Interaction and Mechanisms of Irregular Wear on Wheel and Rail Surfaces. Vehicle Syst Dyn 2003; 40:3–54.
[4] Oostermeijer KH. Review on short pitch rail corrugation studies. Wear 2008;265(9-10):1231–7.
[5] Liang H, Li W, Zhou Z, Wen Z, Li S, An D. Investigation on rail corrugation grinding criterion based on coupled vehicle–track dynamics and rolling contact fatigue model. J Vib Control 2022;28:1176–86.
[6] Hempelmann K, Hiss F, Knothe K, Ripke B. The formation of wear patterns on rail tread. Wear 1991;144:179–95.
[7] Bhaskar A, Johnson KL, Wood GD, Woodhouse J. Wheel-rail dynamics with closely conformal contact Part 1: dynamic modelling and stability analysis. P I Mech Eng F-J Rai 1997;211:11–26.
[8] Afferrante L, Ciavarella M. Short pitch corrugation of railway tracks with wooden or concrete sleepers: An enigma solved? Tribol Int 2010;43(3):610–22.
[9] Wu T, Thompson DJ. Vibration analysis of railway track with multiple wheels on the rail. J Sound Vib 2001;239:69–97.
[10] Frederick CO, A rail corrugation theory. *Proceedings of the 2nd International Conference on Contact Mechanics of Rail-Wheel Systems, University of Rhode Island* (1986) 181-211 (University of Waterloo Press).
[11] Ilias H. The Influence of Railpad Stiffness on Wheelset/Track Interaction and Corrugation Growth. J Sound Vib 1999;227(5):935–48.
[12] Nielsen JCO. Numerical prediction of rail roughness growth on tangent railway tracks. J Sound Vib 2003;267(3):537–48.
[13] Neilsen JB. Evolution of rail corrugation predicted with a non-linear wear model. J Sound Vib 1999;227(5):915–33.
[14] Knothe K, Groß-Thebing A. Short wavelength rail corrugation and non-steady-state contact mechanics. Vehicle Syst Dyn 2008;46:49–66.
[15] Xie G, Iwnicki SD. Calculation of wear on a corrugated rail using a three-dimensional contact model. Wear 2008;265:1238–48.
[16] Feller HG, Walf K. Surface analysis of corrugated rail treads. Wear 1991;144: 153–61.
[17] Baumann G, Fecht HJ, Liebelt S. Formation of white-etching layers on rail treads. Wear 1996;191:133–40.
[18] Wild E, Wang L, Hasse B, Wroblewski T, Goerigk G, Pyzalla A. Microstructure alterations at the surface of a heavily corrugated rail with strong ripple formation. Wear 2003;254:876–83.
[19] Carson RM, Johnson KL. Surface corrugations spontaneously generated in a rolling contact disc. Wear 1971;17:59–72.
[20] Liu Q, Zhang B, Zhou Z. An experimental study of rail corrugation. Wear 2003;255: 1121–6.
[21] Hiensch M, Nielsen JCO, Verheijen E. Rail corrugation in The Netherlands—measurements and simulations. Wear 2002;253:140–9.
[22] Böhmer A, Klimpel T. Plastic deformation of corrugated rails—a numerical approach using material data of rail steel. Wear 2002;253:150–66.
[23] Wen Z, Jin X, Xiao X, Zhou Z. Effect of a scratch on curved rail on initiation and evolution of plastic deformation induced rail corrugation. Int J Solids Struct 2008; 45:2077–96.

[24] Wen Z, Wu L, Li W, Jin X, Zhu M. Three-dimensional elastic–plastic stress analysis of wheel–rail rolling contact. Wear 2011;271:426–36.

[25] Zhao X, Li Z. A three-dimensional finite element solution of frictional wheel–rail rolling contact in elasto-plasticity. P I Mech Eng J-J Eng 2014;229:86–100.

[26] Naeimi M, Li S, Li Z, Wu J, Petrov RH, Sietsma J, et al. Thermomechanical analysis of the wheel-rail contact using a coupled modelling procedure. Tribo Int 2018;117: 250–60.

[27] Wei Z, Núñez A, Boogaard A, Dollevoet R, Li Z. Method for evaluating the performance of railway crossing rails after long-term service. Tribo Int 2018;123: 337–48.

[28] Li Z, Zhao X, Dollevoet R. An approach to determine a critical size for rolling contact fatigue initiating from rail surface defects. Int J Rail Transp 2017;5:16–37.

[29] Li S, Li Z, Dollevoet R. Wear study of short pitch corrugation using an integrated 3D FE train-track interaction model, *The 9th international conference on contact mechanics and wear of rail/wheel systems.* Chengdu: China; 2012. p. 216–22.

[30] Li S, Li Z, Nunez A, Dollevoet R. New insights into the short pitch corrugation development enigma based on 3D-FE dynamic vehicle-track coupled modelling in frictional rolling contact. Appl Sci (Switzerland) 2017;7(8):807.

[31] Li Z, Li S, Zhang P, Núñez A, Dollevoet R. Mechanism of short pitch rail corrugation: initial excitation and frequency selection for consistent initiation and growth. Int J Rail Transp 2022:1–36. https://doi.org/10.1080/23248378.2022.2156402.

[32] Zhang P, Li S, Li Z. Short pitch corrugation mitigation by rail constraint design. Int J Mech Sci 2023;243:108037.

[33] Knothe K, Grassie S. Modelling of railway track and vehicle/track interaction at high frequencies. Vehicle Syst Dyn 1993;22:209–62.

[34] Esveld C. Modern railway track. The Netherlands: MRT-Productions; 2001.

[35] Zhao X, Li Z, Liu J. Wheel–rail impact and the dynamic forces at discrete supports of rails in the presence of singular rail surface defects. P I Mech Eng F-J Rai 2012; 226:124–39.

[36] Benson D, Hallquist J. A single surface contact algorithm for the post buckling analysis of shell structures. Comput Methods in Appl Mech Eng 1990;78:141–63.

[37] Yang Z, Deng X, Li Z. Numerical modeling of dynamic frictional rolling contact with an explicit finite element method. Tribol int 2019;129:214–31.

[38] Zhao X, Li Z. The solution of frictional wheel-rail rolling contact with a 3D transient finite element model: validation and error analysis. Wear 2011;271: 444–52.

[39] Wei Z, Li Z, Qian Z, Chen R, Dollevoet R. 3D FE modelling and validation of frictional contact with partial slip in compression-shift-rolling evolution. Int J Rail Transport 2015;4:20–36.

[40] Oregui M, Li Z, Dollevoet R. An investigation into the vertical dynamics of tracks with monoblock sleepers with a 3D finite-element model. P I Mech Eng F-J Rai 2016;230:891–908.

[41] Molodova M, Li Z, Núñez A, Dollevoet R. Validation of a finite element model for axle box acceleration at squats in the high frequency range. Comput Struct 2014; 141:84–93.

[42] Courant R, Friedrichs K, Lewy H. On the partial difference equations of mathematical physics. Math Ann 1928;11:215–34.

[43] Yang Z, Boogaard A, Chen R, Dollevoet R, Li Z. Numerical and experimental study of wheel-rail impact vibration and noise generated at an insulated rail joint. Int J Impact Eng 2018;113:29–39.

[44] Mises RV. Mechanik der festen Körper im plastisch-deformablen Zustand. Nachrichten von der Gesellschaft der Wissenschaften zu Göttingen, Mathematisch-Physikalische Klasse 1913:582–92.

[45] Bai Y, Wierzbicki T. A new model of metal plasticity and fracture with pressure and Lode dependence. Int J Plast 2008;24(6):1071–96.

[46] Hallquist JO. LS-DYNA Theory Manual, Version 971. USA: Livermore Software Technology Corporation (LSTC), Livermore, CA; 2006.

[47] Li S, Wu J, Petrov RH, Li Z, Dollevoet R, Sietsma J. "Brown etching layer": A possible new insight into the crack initiation of rolling contact fatigue in rail steels? Eng Fail Anal 2016;66:8–18.

[48] Cahoon JR, Broughton WH, Kutzak AR. The determination of yield strength from hardness measurements. Metall Trans 1971;2:1979–83.

[49] Heyder R, Girsch G. Testing of HSH® rails in high-speed tracks to minimise rail damage. Wear 2005;258:1014–21.

[50] Zhou Y, Wang S, Wang T, Xu Y, Li Z. Field and laboratory investigation of the relationship between rail head check and wear in a heavy-haul railway. Wear 2014;315:68–77.